Structure of Ce_2RhIn_8: an example of complementary use of high-resolution neutron powder diffraction and reciprocal-space mapping to study complex materials

E. G. Moshopoulou,[a]* R. M. Ibberson,[b] J. L. Sarrao,[c] J. D. Thompson[c] and Z. Fisk[c]

[a]National Center for Scientific Research 'Demokritos', Institute of Materials Science, 15310 Agia Paraskevi, Greece, [b]ISIS Facility, CCLRC-Rutherford Appleton Laboratory, Chilton, Didcot, Oxon OX11 0QX, England, and [c]Los Alamos National Laboratory, MST-10, MS K764, Los Alamos, NM 87545, USA

Correspondence e-mail:
evagelia@ims.demokritos.gr

The room-temperature crystal structure of the heavy fermion antiferromagnet Ce_2RhIn_8, dicerium rhodium octaindide, has been studied by a combination of high-resolution synchrotron X-ray reciprocal-space mapping of single crystals and high-resolution time-of-flight neutron powder diffraction. The structure is disordered, exhibiting a complex interplay of non-periodic, partially correlated planar defects, coexistence and segregation of polytypic phases (induced by periodic planar 'defects'), mosaicity (*i.e.* domain misalignment) and non-uniform strain. These effects evolve as a function of temperature in a complicated way, but they remain down to low temperatures. The room-temperature diffraction data are best represented by a complex mixture of two polytypic phases, which are affected by non-periodic, partially correlated planar defects, differ slightly in their tetragonal structures, and exhibit different mosaicities and strain values. Therefore, Ce_2RhIn_8 approaches the paracrystalline state, rather than the classic crystalline state and thus several of the concepts of conventional single-crystal crystallography are inapplicable. The structural results are discussed in the context of the role of disorder in the heavy-fermion state and in the interplay between superconductivity and magnetism.

1. Background

The combined effect of correlations and disorder on the ground state, physical properties and phase transitions of solids has intrigued condensed matter scientists for more than four decades. The effect is especially relevant in a subset of intermetallic compounds and alloys containing *f*-electron elements, most commonly Ce, U or Yb. In these materials the strong coupling between the conduction electrons and the local *f*-electron moment fluctuations enhances considerably the effective mass of the conduction electrons and produces unexpected low-temperature properties. Even in the absence of disorder, these so-called heavy fermion materials are unconventional solids in the sense that their properties are not anticipated within the conceptual framework containing the band theory, the phonon-mediated theory of conventional superconductivity and the spin-wave theory of solids. Stewart (1984), Fisk *et al.* (1987), Fisk, Hess *et al.* (1988), Fisk, Thompson & Ott (1988), Fisk, Sarrao *et al.* (1995), Ott & Fisk (1989), Grewe & Steglich (1991), Aeppli & Fisk (1992), Thompson & Lawrence (1994) and King (1997) review the physics and chemistry of heavy fermion materials. The presence of even weak (by metallurgical standards) disorder has dramatic effects on the properties of these systems, hence detecting and understanding the type, strength and spatial

research papers

extent of disorder is essential for determining their underlying physics. The reason for this sensitivity of the heavy fermion materials to disorder involves their very basic physics and energy scales. The local spins in these materials, coupled *via* the exchange parameter J to the conduction electrons, are compensated below a small energy scale, the Kondo temperature, T_K, which depends exponentially on $|J|$. There is an obvious competition between the low-temperature compensated state and the magnetically ordered state of the uncompensated moments. The energy scale of the latter is the Ruderman–Kittel–Kasuya–Yosida (RKKY) temperature, T_{RKKY}, which characterizes the moment–moment interaction in metals and changes as $|J|^2$. The competition between the single-site Kondo screening and inter-site RKKY spin coupling depends on, besides $|J|$, the density of the conduction electrons and on the spatial dimensionality. It has been demonstrated by Bernal *et al.* (1995) and Miranda and co-workers (Miranda *et al.*, 1997; Miranda & Dobrosavljevic, 2001) that modest disorder leads to modest variations of J which, because it is amplified exponentially, can lead to wide distributions of T_K and thus to dramatic changes of the low-temperature properties. This concept forms the basis of the 'Kondo disorder model' (Miranda *et al.*, 1996, 1997; Miranda & Dobrosavljevic, 2001), which is one of the two main classes of theories ('single ion' and 'cooperative behavior' approaches) addressing the role of disorder in the quantum critical point (QCP) and non-Fermi liquid behavior of heavy fermion materials. According to the second class of theories, namely the 'magnetic Griffiths phase approach' (Castro Neto *et al.*, 1998; Castro Neto & Jones, 2000), there is also a broad distribution of T_K, but close to the QCP, in the paramagnetic phase, finite clusters of magnetically ordered atoms can fluctuate quantum mechanically. In this case, the so-called quantum Griffiths–McCoy singularities are generated and lead to zero-temperature divergences of the physical quantities. Theoretical predictions from both these approaches are most commonly compared with experimental results from materials exhibiting chemical disorder caused by doping, since doping is a rather standard way to bring these systems to the QCP and to induce non-Fermi liquid behavior. While this synergy between experiment and theory provided us with significant results, identifying or discovering heavy fermion materials that exhibit other types of disorder and characterizing accurately their structure and properties should challenge and hence advance our present understanding of the interplay between disorder and correlations. The study of the relatively new heavy fermion material Ce_2RhIn_8 offers the promise of progress in this regard, since this material adopts an unusual (for a heavy fermion) disordered crystal structure and exhibits some remarkable low-temperature properties.

Ce_2RhIn_8 is a member of the linear homologous series of heavy fermion materials $Ce_mT_nIn_{3m+2n}$, where $m = 1, 2; n = 0, 1; T = Co, Rh, Ir$. These materials adopt tetragonal crystal structures built by monolayers (for $m = 1$) or bilayers (for $m = 2$) of face-sharing cuboctahedra $[CeIn_3]$, and monolayers (for $n = 1$) of edge-sharing rectangular parallelepipeds $[TIn_2]$ stacked alternatively in the [001] direction (Grin *et al.*, 1979;

Moshopoulou *et al.*, 2001; Moshopoulou, Prokes *et al.*, 2002; Macaluso *et al.*, 2003). The series has attracted considerable interest over the last five years, not only because of the interesting low-temperature properties of its members but also because it allows investigation of the role of spatial dimensionality in controlling the heavy-fermion state and the cooperative phenomena of unconventional superconductivity and magnetism.

The first evidence that the crystal structure of Ce_2RhIn_8 deviates from the idealized crystal structure came from powder laboratory X-ray diffraction data. The powder pattern of ground crystals could be indexed unambiguously, assuming the compound to be of the Ho_2CoGa_5-type structure (Grin *et al.*, 1979), space group $P4/mmm$ and $Z = 1$. However, comparison of the observed diagram with the calculated one revealed that the observed intensities of several peaks, mainly (*hhl*), were different from the calculated ones even after taking into consideration the effects of the atomic displacements, preferred orientation and absorption. Prompted by this observation, and in order to check for weak effects like diffuse scattering or superstructure, which would be hardly observable by conventional powder X-ray diffraction, we carried out preliminary electron diffraction experiments. The electron diffraction patterns revealed the presence of weak diffuse streaks between the Bragg spots, along the [001]* direction in the reciprocal plane (*a*c**). Such diffuse streaks are typical of the presence of planar defects with the planes being perpendicular to the [001] direction. No diffuse streaks or other type of diffuse scattering were observed on the reciprocal plane (*a*b**). In addition, several Bragg peaks appeared to be rather elongated (but not split), indicating the presence of slightly disoriented adjacent domains and/or slight local variations of the cell parameters. Whereas the preparation of thin, 'electron-beam transparent' specimens can in some cases induce defects in the specimen, the electron diffraction data taken together with the powder diffraction results imply that the structure of Ce_2RhIn_8 is affected by disorder. The preliminary data just described provided the first evidence of the true structural complexity of Ce_2RhIn_8 and were critical to our choice of the appropriate diffraction methods that enabled a thorough structural characterization of this material.

Additional indications that the structure of Ce_2RhIn_8 might exhibit disorder stem from some of its low-temperature properties and parameters. Ce_2RhIn_8 is a heavy fermion antiferromagnet with the Sommerfeld coefficient $\gamma \simeq 400 \, mJ \, mol^{-1} \, CeK^2$ and Néel temperature $T_N = 2.8 \, K$ (Thompson *et al.*, 2001). Below T_N, the magnetic structure of the material is collinearly antiferromagnetic (Bao *et al.*, 2001). In addition, a different magnetic structure appears below $T_{LN} = 1.65 \, K$ (Malinowski *et al.*, 2003; Morris *et al.*, 2004; Bao, 2005; Ueda *et al.*, 2004). The application of the magnetic field parallel to the *ab* plane induces both first- and second-order phase transitions at low temperatures and at least three phases with different magnetic structures appear below 3 K (Cornelius *et al.*, 2001; Moshopoulou, Sarrao *et al.*, 2002). Whether these additional magnetic phases (in the absence or presence of a field) stem totally from the principal collinear anti-

ferromagnetic phase or are signatures of other chemical phases (very similar with the principal one) that simply order at different temperatures is at present an open question. The resistivity measurements also provide some indications that structural inhomogeneities might exist in the material. While no bulk superconductivity was found by specific heat or magnetization measurements at ambient pressure, the resistivity drops to zero below 0.6 K in some samples (Ueda *et al.*, 2004). Resistivity (Nicklas *et al.*, 2003; Ohara *et al.*, 2003), *ac* susceptibility (Ueda *et al.*, 2004) and ongoing specific heat measurements (Lengyel *et al.*, 2004) under pressure revealed that Ce_2RhIn_8 becomes a superconductor above 16.3 kbar with the critical temperature T_c = 2 K. The temperature–pressure phase diagram shows that superconductivity and magnetism coexist over an extended pressure interval. This diagram is rather different from the corresponding diagrams of other heavy fermion materials, such as $CeIn_3$ and $CePd_2Si_2$ (Marthur *et al.*, 1998) and $CeRhIn_5$ (Hegger *et al.*, 2000; Llobet *et al.*, 2004). Interestingly, the ambient-pressure residual resistivity ρ_0 of Ce_2RhIn_8 is one to two orders of magnitude higher than the ρ_0 value of the other members of the series, $Ce_mRh_nIn_{3m+2n}$, *i.e.* $CeIn_3$ and $CeRhIn_5$, which typically have $\rho_0 \simeq 1 \ \mu\Omega$ cm. The high value of ρ_0 is reported independently by different groups (Nicklas *et al.*, 2003; Ueda *et al.*, 2004) and it is reproduced in all of the many crystals of Ce_2RhIn_8 studied and therefore appears to be an intrinsic property of this compound (Nicklas *et al.*, 2003; Ueda *et al.*, 2004). The value of the residual resistivity reflects scattering from random defects in the material (such as dislocations, impurities, anti-phase boundaries, random anti-site disorder, planar defects, misaligned mosaic blocks *etc.*) that obviously break the translation symmetry. Nearly periodic 'disorder' might have no or very little effect on the residual resistivity. For example, in the heavy fermion compound $CeInCu_2$, nearly periodic 'disorder' (observed as almost periodically modulated diffuse intensity in reciprocal space) does not influence the residual resistivity, even if it remains at low temperature (Takahashi *et al.*, 1999). As ρ_0 varies with pressure, pressure-dependent spin fluctuation scattering also likely contributes to this large value of ρ_0 (Nicklas *et al.*, 2003).

This paper reports the disordered structure of the heavy fermion material Ce_2RhIn_8, deduced from high-resolution diffraction experiments, namely synchrotron X-ray reciprocal-space mapping of single crystals and time-of-flight neutron powder diffraction. Besides establishing the crystal structure and comparing it with those of $CeIn_3$ and $CeRhIn_5$, the principal aim of this study is to determine in detail the type(s) of disorder that the material exhibits. Given the important role of disorder in the physics of heavy fermion materials, this structural study can provide critical information for understanding the properties of the material, for testing existing theoretical models and eventually for suggesting new directions for the theory.

The article is organized as follows: because of the wide variety of the types of disorder, we first summarize in the next section some basic theoretical considerations on disorder and especially on the disorder types that affect the structure of

Ce_2RhIn_8. In the same section we also briefly compare some diffraction methods which are used to assess the crystal quality and the deviations from perfect order. The concepts presented in §2 are the basis for the interpretation of our experimental data and will be often used in §§3, 4 and 5. In §3 we describe our experimental procedure. The results obtained are discussed in §4. Finally, the concluding remarks of this study are given in §5.

2. Main theoretical considerations

2.1. Types of disorder and correlation length

The ideal crystalline solid is a periodic and infinite repetition of identical groups of atoms in space, with well defined stoichiometry, unit cell and space-group symmetry, and with a crystal structure which represents a unique free-energy minimum in local parameter space. Structural information on such materials is almost routinely obtained by the well established techniques of X-ray and neutron diffraction in conjunction with powerful structural-analysis algorithms. While this concept of solids represents one of the pillars in the construction of condensed matter science, it is also true that a vast majority of real materials are structurally flexible or adaptive phases whose chemistry and/or crystallinity (degree of order) cannot be expressed in conventional crystallographic form. The characteristic parameter which characterizes such disordered crystalline structures in real space is the correlation length, *i.e.* the length over which it is possible to predict the location of the next repeat unit based on the lattice parameters. It is thus quite common to consider the limiting cases of this parameter: long-range disorder (*e.g.* mosaicity, strain *etc.*) and short-range disorder (*e.g.* anti-site, displacive disorder *etc.*) in direct space (Schwartz & Cohen, 1987). In general, long-range phenomena in real space will give localized effects in reciprocal space, while short-range phenomena in direct space will be revealed by extended effects in reciprocal space. Thus, long-range disorder will affect the distribution of the intensity in the immediate vicinity of reciprocal lattice points (RLPs), *i.e.* the shape of the Bragg peaks, and as a result, long-range disordered crystals will give diffraction patterns consisting only of Bragg reflections broadened in various directions of reciprocal space. In contrast, the signature of short-range disorder on the diffraction patterns of a crystal is the existence of a weak but highly structured diffuse intensity distributed more or less uniformly throughout reciprocal space and accompanying the strong, highly symmetric and localized (on the RLPs) Bragg reflections of an underlying average structure. The case of real disordered crystals is often akin to the situation combining both these limits.

For relatively simple structures and defect configurations, the distribution of the diffracted intensities in reciprocal space (*i.e.* Bragg and diffuse scattering) and of the intensity variations within the Bragg peaks can be predicted theoretically with reasonable accuracy. For this purpose, two theories starting from rather opposite viewpoints about the crystalline material have been employed: the dynamic theory and the

research papers

kinematic (or mosaic) theory. The dynamic theory of diffraction from disordered crystals starts from a perfect crystal, then introduces a small number of well defined defects (such as vacancies, dislocations, stacking faults) and calculates the diffracted intensities from first principles. This theory predicts rather accurately the microscopic intensity variations within the Bragg peaks of almost perfect materials; however, it is inapplicable for crystals with high defect density, such as is the case for the material we discuss in this work. Such materials can be approximated by the kinematic theory. The starting model here is a crystal composed of a large number of microscopic regions (mosaic blocks) of perfectly ordered material assembled into a microscopic object in such a way that there are small misorientations between the perfect blocks. It is then possible to introduce, besides mosaicity, additional disorder (e.g. planar defects, substitutional disorder, strain etc.) within each perfect mosaic block. The boundaries between such regions are ignored and no model for them is proposed. The kinematic theory predicts quite accurately the effects of each type of simple defects on the diffracted intensity. Consequently, common types of defects (such as mosaicity, strain, planar defects, substitutional disorder etc.) can be identified from very precise and detailed diffraction data. However, the kinematic theory cannot calculate accurately complex defect structures (e.g. combinations of defects) or the morphology of complex real materials.

2.2. Disorder types relevant to Ce_2RhIn_8: planar defects, mosaicity, strain

The next few paragraphs show that the structure of Ce_2RhIn_8 is affected by an interplay of both short- and long-range disorder effects: planar defects (random and periodic), mosaicity (i.e. domain misalignment) and non-uniform strain. It is therefore instructive to briefly present here how these types of disorder are manifested in reciprocal space, according to kinematic theory (Schwartz & Cohen, 1987). Reciprocal space is expressed in terms of $q_\parallel$ and $q_\perp$, which are the vectors parallel and perpendicular to the scattering vector (or reciprocal lattice vector) respectively.

A mosaic structure is usually produced by dislocations and/or planar defects grouped in some array, causing regions of the crystal to tilt slightly with respect to other regions. The presence of such block misalignment implies that the crystal consists of many small domains diffracting independently. The mosaicity of the crystal is described by three parameters, the angular spread ω of the mosaic blocks, the size s of the blocks and the variation $\delta\alpha$ in the cell dimensions between different blocks (Nave, 1998). Each of these parameters contributes to the observed Bragg reflection in the following way. The angular spread ω of the mosaic blocks creates spherical caps instead of points in reciprocal space which, as they pass through the sphere of reflection, project to a flat detector to give arcs of angular width ω. The finite size s of the blocks causes broadening of the Bragg reflections over the angle λ/s. As this broadening is independent of the interatomic distance

d, the finite size s therefore causes the same broadening of the diffracted beam at any distance from the center of reciprocal space. The variation in cell dimensions, i.e. non-uniform strain, originates from inhomogeneous elastic deformations of the crystal, which cause the lattice parameter to be a function of position in the crystal. In the absence of the previous parameter the two other parameters of mosaicity (ω and s), i.e. if the crystal consists of large and well aligned but strained blocks, the X-ray or neutron beam samples all lattice parameters. Consequently, the variation in the cell dimensions $\delta\alpha/\alpha$ will give a broadening of $(\lambda/d)(\delta\alpha/\alpha)$, which obviously increases with distance from the center of reciprocal space due to the $1/d$ factor in this expression. Therefore, the effects of finite size s of the mosaic blocks and the variation in the cell dimensions between blocks can be distinguished by the evolution of the broadening of the Bragg reflections as a function of the distance from the origin of reciprocal space. In addition, the arcs on the detector, created by an angular mosaic spread, can be distinguished by inspection from the broadening of the Bragg reflections caused by a variation in the cell dimensions between blocks: the latter effect causes the spots to increase in size radially as well as azimuthally.

We now turn to consider how planar defects are revealed in reciprocal space. Planar defects occur in a crystal structure when one crystallographic plane is displaced from another by a lattice vector, which is different from its Bravais lattice vector in the perfect crystal. The effects of the planar defects on the diffraction patterns are quite pronounced and include unusual shifts of the position of particular Bragg peaks, hkl-dependent and asymmetric peak broadening, diffuse streaks (with possible intensity modulations) in the reciprocal direction parallel to the layers. Thus, both long- and short-range disorder signatures appear in reciprocal space. For planar defects, the peak broadening is due to 'particle size' effects, where 'particle size' is the spacing between the stacking faults. The difference in broadening of different hkl reflections is characteristic of planar defects. Simple 'mosaic block size' causes all Bragg peaks to broaden in the same manner.

2.3. Assessment of crystal quality and reciprocal-space mapping

A mandatory first step for the structural characterization of a new single crystalline material is to assess its degree of perfection by checking the shape of the Bragg peaks and searching for the presence of diffuse scattering in reciprocal space. If the Bragg peaks are not unusually broadened and there is no diffuse scattering among them, then the crystal approaches perfection and consequently its crystal structure can be deduced accurately from an analysis of the Bragg intensities collected by conventional single-crystal X-ray or neutron diffraction.

A quick assessment of the crystal quality, before an X-ray or neutron diffraction experiment, is commonly done by electron diffraction in combination with rocking-curve measurements. For materials stable under the electron beam, electron

diffraction can disclose the presence of the diffuse scattering in reciprocal space and hence short-range disorder in the crystal. Rocking-curve studies, on the other hand, analyze the angular range of a reflection and thus can reveal the long-range disorder (*e.g.* mosaicity, strain *etc.*) in the material. The crystal, initially set to the Bragg position, is then rotated ('rocked') through the Bragg angle. If mosaic blocks with various orientations and/or regions with slightly different lattice parameters (owing to non-uniform strain, planar defects *etc.*) are present in the irradiated area of the crystal, through 'rocking' they are all brought successively into their exact Bragg positions and reflect in slightly different Bragg angles. The resulting curve of intensity *versus* θ ('rocking curve') is a convolution of the sample and instrument parameters, *i.e.* geometric and spectral divergence. The instrument parameters are routinely deconvoluted and the width of the rocking curve is a measure of mosaicity and/or *d*-spacing variations in the crystal, *i.e.* the crystal quality. Rocking-curve measurements cannot however separate the effects arising from the distribution of sizes and orientations of the mosaic blocks from those originated from the *d*-spacing distribution in the crystal, because for each angle the measured intensity is effectively integrated over a relatively wide range of reciprocal space.

To overcome this limitation and to reach a microscopic understanding of the intricate disorder effects present in complex materials such as that discussed in this work, we use the so-called reciprocal-space mapping (RSM) technique (Fewster, 1997). RSM is a high-resolution, high-intensity technique used for mapping reciprocal space in great detail *inside* and *around* the Bragg reflection. RSM differs from the rocking-curve technique in that the range of integration over reciprocal space is considerably reduced. This is achieved by inserting a third 'analyzer' crystal (made of the same material as the monochromator) in front of the detector of the two-axis diffractometer used for rocking-curve measurements. The set-up, termed a triple-axis diffractometer (Brockhouse, 1955), consists of the monochromator, the sample and the analyzer and can provide high resolution in directions both parallel and perpendicular to the scattering vector. Appropriate rotations of the sample and analyzer crystal allow undistorted and detailed maps to be recorded of reciprocal space in two or three dimensions and the effects arising from mosaicity to be deconvoluted from those due to other effects like planar defects and/or strain. The technique of RSM using the triple-axis diffractometry and conventional X-rays has long been known (Pick *et al.*, 1977). However, RSM more recently became a very powerful tool for the assessment of crystal perfection and investigations of structural inhomogeneities by the use of medium- or high-energy synchrotron X-rays. Such radiation combines, among other properties, the advantage of low attenuation (*i.e.* high penetration ability) with high resolution at large momentum transfers. Thus, it allows us to probe even weak disorder in bulk materials without having to account for absorption and surface effects, and with reciprocal-space resolution significantly better than the best laboratory-based experiments.

3. Experimental

3.1. Synthesis

Single crystals of Ce_2RhIn_8 were prepared by the flux technique (Fisk & Remeika, 1989; Canfield & Fisk, 1992) using an In flux. High-purity (99.95% or better) stoichiometric ratios of Ce and Rh together with excess In were placed in an alumina crucible, which was then encapsulated in an evacuated quartz tube. The resultant ampoule was heated over several hours to 1373 K, allowed to equilibrate for 2 h, and then cooled with a rate of 8 K h^{-1} to 973 K. At this point, the excess flux was decanted in a centrifuge, leaving well separated single crystals. Most crystals were plate-like with the tetragonal axis perpendicular to the plate.

3.2. High-resolution synchrotron X-ray RSM

The aim of the RSM experiments was to assess the degree of deviation of the structure of Ce_2RhIn_8 from perfect order and to determine the types of disorder from the distribution of the intensity inside, around and between the Bragg peaks.

RSM experiments were carried out on the high-resolution single-crystal diffraction station 16.3 (Collins *et al.*, 1998, 1999; Murphy *et al.*, 2001) at the Synchrotron Radiation Source, Daresbury Laboratory, UK. Station 16.3 is situated on a beamline employing a 6 Tesla superconducting wavelength shifter (SRS Wiggler 16), which provides photon beams with a range of energies from 5 to 70 keV. An important design characteristic of the station is that there are no focusing optics, largely to preserve the beam polarization, collimation and energy range (at the expense of flux). Such highly collimated intense beams in combination with the triple-axis geometry make this station particularly well suited for high-resolution applications. The station has a large vertically deflected six-circle diffractometer situated 32 m from the wavelength shifter and equipped with a displex closed-cycle cryostat for measurements in the temperature range from 281 to 573 K. The white beam was monochromated by either one or two channel-cut silicon crystals. The sample was mounted on a φ axis riding on a χ circle, which turns about the ω axis. The diffracted beam entered the detector *via* a two- or three-reflection Si(111) analyzer that turns about the 2θ axis. All axes had an accuracy (largest angular error) of $10^{-4\circ}$ and a resolution (minimum step) of the same order of magnitude.

A plate-like single crystal of Ce_2RhIn_8 with well defined faces was selected for our experiments. The RSM scans were performed from room temperature down to 8.2 K by mounting a Displex cryostat to the Eulerian cradle of the diffractometer. A wavelength of 1 Å, *i.e.* energy of 12.398 keV, was chosen, since this energy corresponds to the maximum flux $[1.2 \times 10^{10}$ photons mm^{-2} s^{-1} (200 mA)$^{-1}$ (0.1% bandwidth)$^{-1}$] according to the flux spectrum at station 16.3 (Collins *et al.*, 1998). Moreover, wavelengths of 1 Å or lower are preferable to minimize absorption, extinction and polarization effects. After aligning the crystal and centering it in the beam, several strong reflections were identified and used for the determination of the orientation matrix. Then, through

appropriate automatic rotations around the φ, χ and ω axes, the crystal was brought successively into various Bragg positions. Preliminary rocking-curve measurements of the resultant diffraction peaks were carried out in a two-axis mode to check the sample quality from the profile and full-width at half-maximum of the peaks, and to select the beam size and the width of the slits. The crystal appeared single (no twins or crystallites stuck on the crystal were detected), but the peaks were definitely broad. A beam size of 2 mm horizontally and vertically was used for all the measurements. The sizes of the detector slits and of the beam-defining slits were optimized to provide a low background, but good k-space resolution without sacrificing significant incident and diffracted intensity. A Si(111) channel-cut monochromator, a Si(111) analyzer and a solid-state Ge detector were used for the whole data collection.

A series of high-resolution, two-dimensional reciprocal-space maps were collected surrounding several 00l, 0kl, hkl reflections. The choice of the reflections was based on the following two considerations. First, our preliminary electron diffraction experiments and the fact that the structure is tetragonal suggested that there are planar defects (with the planes being perpendicular to the tetragonal axis), affecting at least the (00l) reflections. Consequently, these reflections were investigated in more detail. Second, it is expected that planar faults would cause long-range disorder (*i.e.* mosaicity, strain) to some extent. To investigate and distinguish these effects, it was necessary to check the distribution of the intensity both parallel and perpendicular to the diffraction vector and measure several diffraction orders accessible by the diffractometer.

To map out the area of reciprocal space around a desired reflection, initially we brought (through appropriate rotations of the crystal) the desired reciprocal lattice point into contact with the Ewald sphere of reflection. Then we collected grid scans, *i.e.* plots of the intensity distribution on a 'grid' defined by 2θ *versus* $\varepsilon = \omega - \theta$. As the peak profile of the reflections was found to be quite complex, several of the grid scans, *i.e.* the reciprocal-space maps of the reflections were collected in both bisecting and non-bisecting modes. The arrangement of the diffractometer is in bisecting mode when the χ circle bisects the angle between the incident and the diffracted beams. In this case, $\omega = \theta$, thus $\varepsilon = 0$ (Arndt & Willis, 1966; Stout & Jensen, 1989; Brock *et al.*, 1995; Schwartz & Cohen, 1987; Baruchel *et al.*, 1993). Obviously, the angle $\varepsilon = \omega - \theta$ is the departure from the bisecting condition. All peaks were scanned along or in a direction parallel to the scattering vector by coupled rotations of the crystal and the detector, allowing in this way complex intensity distributions to be measured accurately. This so-called $\omega - 2\theta$ scan moves through reciprocal space in the radial direction, *i.e.* along a line starting from the origin of reciprocal space and passing through the reflection. For the control of the diffractometer and the data acquisition, we used the instrument software *PINCER*. On completion of a scan, the data were visualized using *MATLAB*, which was set up to work in conjunction with *PINCER* to produce automatic data plots and data analysis.

3.3. High-resolution neutron powder diffraction

As will be shown in the next section, the high-resolution synchrotron X-ray reciprocal-space-mapping experiments just described provided us with critical but qualitative information about the types of disorder that affect the structure of Ce_2RhIn_8. In order to accurately determine the structure and thus to gain quantitative information on the structural parameters that are critical for the properties of the material, we carried out high-resolution powder neutron diffraction experiments.

For the neutron experiments we used the high-resolution powder diffractometer (HRPD; Ibberson *et al.*, 1992) at the ISIS Facility, Rutherford Appleton Laboratory, UK. HRPD operates on the time-of-flight principle, using a pulsed polychromatic neutron beam generated by the spallation process. Neutron wavelengths were discriminated by their arrival time since $t \propto 1/v_n \propto \lambda_n \propto d$, where t is the time of flight, v_n is the neutron velocity, λ_n is the neutron wavelength and d is the d spacing of a particular Bragg reflection. The data were recorded by fixed-angle detectors. For diffraction experiments, the resolution of the diffractometer, $\Delta d/d$, was of paramount importance in revealing subtle structural details and accurately determining the crystal structure. $\Delta d/d$ is a measure of the spread in the Bragg reflection for a given d spacing. HRPD permits routine data collection with a resolution of $\Delta d/d \simeq 4 \times 10^{-4}$ in the main backscattering detector bank. Moreover, such high-resolution data may be collected for Bragg reflections at d spacings of well below 1 Å. This combination of high $\sin \theta/\lambda$ and very high resolution is the principal factor that enabled HRPD to provide an alternative to single-crystal neutron or X-ray diffraction for obtaining both accurate and precise structural parameters in moderately complex structures. Although a conventional X-ray single-crystal diffraction experiment has access to directional information in three dimensions and the intensities of resolved diffraction maxima, departures from the ideal symmetry of the main phase are commonly only a few standard deviations and therefore cannot be resolved. On HRPD such departures from ideal symmetry can be resolved due to the very high resolution of the instrument, and they are observed as peak splitting and/or broadening. The technique is thus particularly suited in cases of materials containing multiple, structurally similar phases such as the material investigated in this work.

For the high-resolution powder neutron diffraction experiment, several single crystals of Ce_2RhIn_8 (taken from the same batch as that used for the RSM experiment) were hand-ground and sifted; from the resulting fine powder, 2.0139 g were loaded in a $15 \times 20 \times 2$ mm^3 holder. These dimensions were optimal to minimize absorption effects. Data were collected at room temperature for *ca* 12 h to obtain high-quality statistics. The data were recorded at the backscattering bank, which is at $168°$ with respect to the incident beam. Under these experimental settings, the diffraction data have an approximately constant resolution of $\Delta d/d = 8 \times 10^{-4}$. A standard data reduction procedure was followed: the data were normalized to the incident-beam monitor profile and

corrected for detector efficiency effects using a previously recorded vanadium spectrum.

4. Results and discussion

4.1. Reciprocal-space maps

Fig. 1(a) shows grid scans of 2θ *versus* $\varepsilon = \omega - \theta$ which map out an area of reciprocal space around the 002 reflection at room temperature. The corresponding peak profile is given in Fig. 1(b). The scan was taken at the bisecting position, *i.e.* $\omega = \theta$. The horizontal axis of Fig. 1(a) is the direction of the $\omega - 2\theta$ scan, *i.e.* the direction of the diffraction vector. The broadening of the 002 reflection perpendicular to the scattering vector implies that the crystal structure consists of misaligned mosaic blocks. The pronounced diffuse streaks along the (002)* reciprocal lattice vector are characteristic of planar defects with the planes being perpendicular to the c axis.
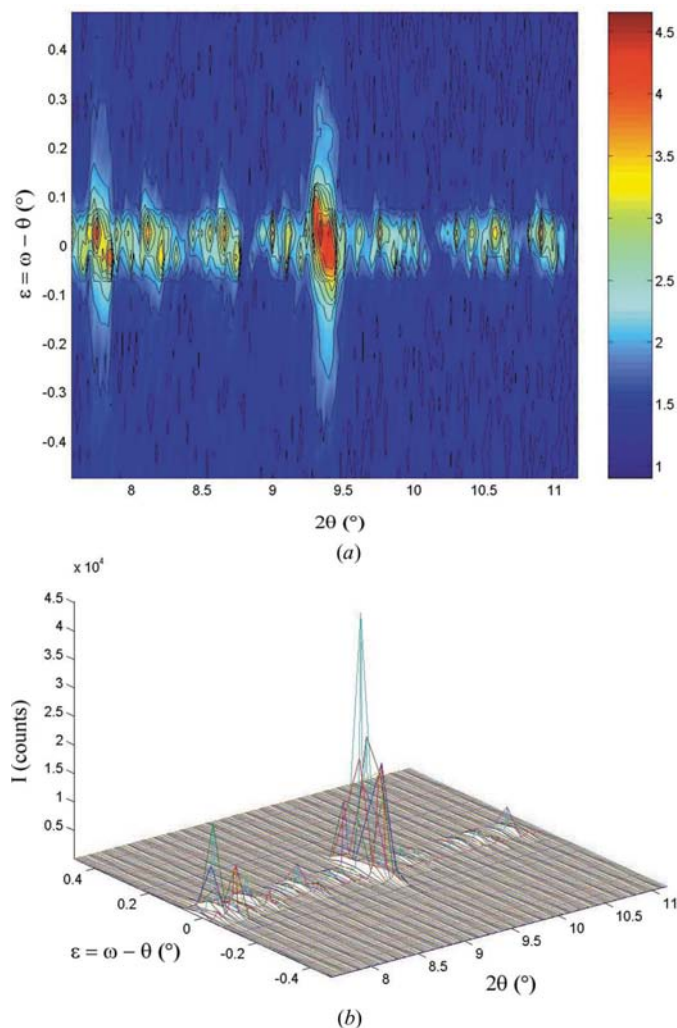
Furthermore, at the reciprocal lattice point 002 coexist more than one Bragg peaks 002 with different intensities. The first question that arises from this map is whether at least some of the minor peaks stem from crystallites attached to the crystal. Given that the crystal was aligned and centered in the beam at the beginning of the experiment, and then brought at Bragg position, it is unlikely that small crystallites randomly stuck on the crystal are also at Bragg position. The most reasonable explanation is that the crystal is single, but consists of misaligned mosaic blocks; the most tilted ones are responsible for these multiple peaks. However, given the presence of planar defects and the concomitant local strain variations, it is also possible that, in addition to mosaicity, the material is also structurally inhomogeneous, *i.e.* it probably consists of component phases having different fractions and slightly different lattice constants. To better investigate these
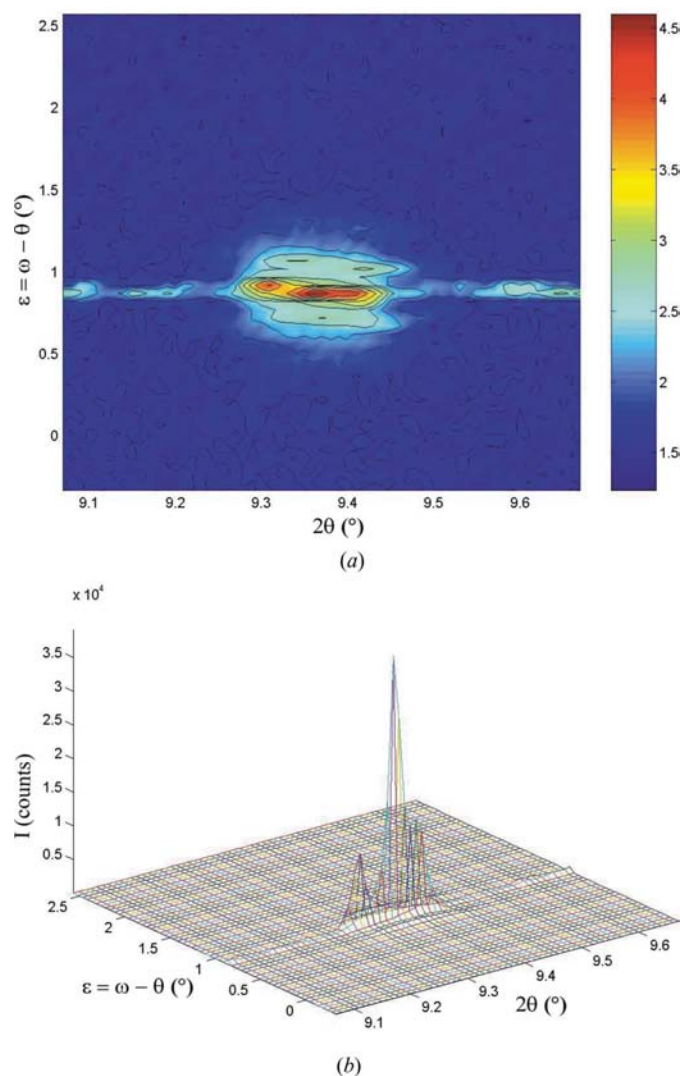

Figure 1
(a) Reciprocal-space map and (b) the corresponding peak profile of the 002 reflection at room temperature. The horizontal axis of (a) is the direction of the $\omega - 2\theta$ scan (direction of the diffraction vector), and the vertical axis of (a) is the offset in the ω-scan direction [$\varepsilon = (2\theta/2) - \omega$]. The map was taken at the bisecting setting, *i.e.* $\omega = \theta$. The color scale is logarithmic to base 10.

Figure 2
(a) Reciprocal-space map and (b) the corresponding peak profile of the 002 reflection at room temperature. The horizontal axis of (a) is the direction of the $\omega - 2\theta$ scan (direction of the diffraction vector) and the vertical axis of (a) is the offset in the ω-scan direction [$\varepsilon = (2\theta/2) - \omega$]. The map was taken at the non-bisecting setting, *i.e.* $\omega \neq \theta$. The color scale is logarithmic to base 10.

scenarios and because of the complex shape of the peak, an additional scan was taken at a non-bisecting position (Figs. 2a and b). This map reproduces the basic features revealed by the previous map. While it cannot be used to obtain absolute lattice parameters because of the broadness of the peaks, it provides qualitative information on the types of disorder. The streaks and the broadening of the peak in the direction parallel to the diffraction vector again imply the presence of planar defects. Strain as well as small and well aligned mosaic blocks can also be partially responsible for the peak broadening parallel to the diffraction vector. To investigate if only mosaicity is responsible for such multiple peaks, we checked the evolution of the relative intensity of the coexisting peaks as a function of temperature. Figs. 3(a), (b) and 4(a), (b) show the reciprocal-space maps of the 002 reflection at 100 and 8.2 K, respectively, obtained under identical experimental conditions as the room-temperature map. If the crystal was not single and crystallites stuck on the crystal were responsible for the weak peaks, then at low temperature the intensities of all the peaks would become lower, but the angular distribution of the peaks and their relative intensities should remain the same as at room temperature. In that case, the weak peaks and especially that at low 2θ would become weaker, but (considering the variation of the intensity of the main peak) should be observable at 100 K. Even if we still assume that the crystal is not single and the weak peaks simply become immeasurably small at 100 K, the change of the profile of the main peak is counter to expectation. These observations substantiate the conclusion drawn from Fig. 1 that the crystal is single, but adopts a mosaic structure. The decrease of temperature might cause some rearrangement of the mosaic blocks and thus the angular distribution of the various peaks can be slightly different from that at room temperature. Indeed, the angular distribution of the intensities collected at room temperature is different from that of those collected at 100 K, but then it
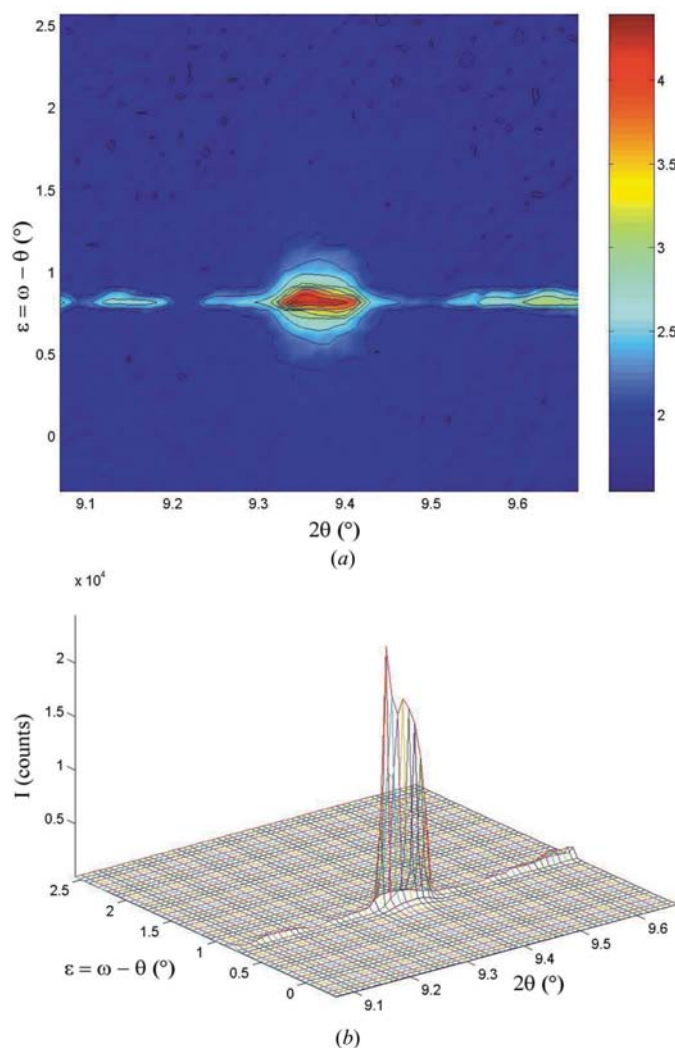

Figure 3
(a) Reciprocal-space map and (b) the corresponding peak profile of the 002 reflection at 100 K. The horizontal axis of (a) is the direction of the ω–2θ scan (direction of the diffraction vector) and the vertical axis of (a) is the offset in the ω-scan direction [$\varepsilon = (2\theta/2) - \omega$]. The map was taken at the non-bisecting setting, i.e. $\omega \neq \theta$. The color scale is logarithmic to base 10.
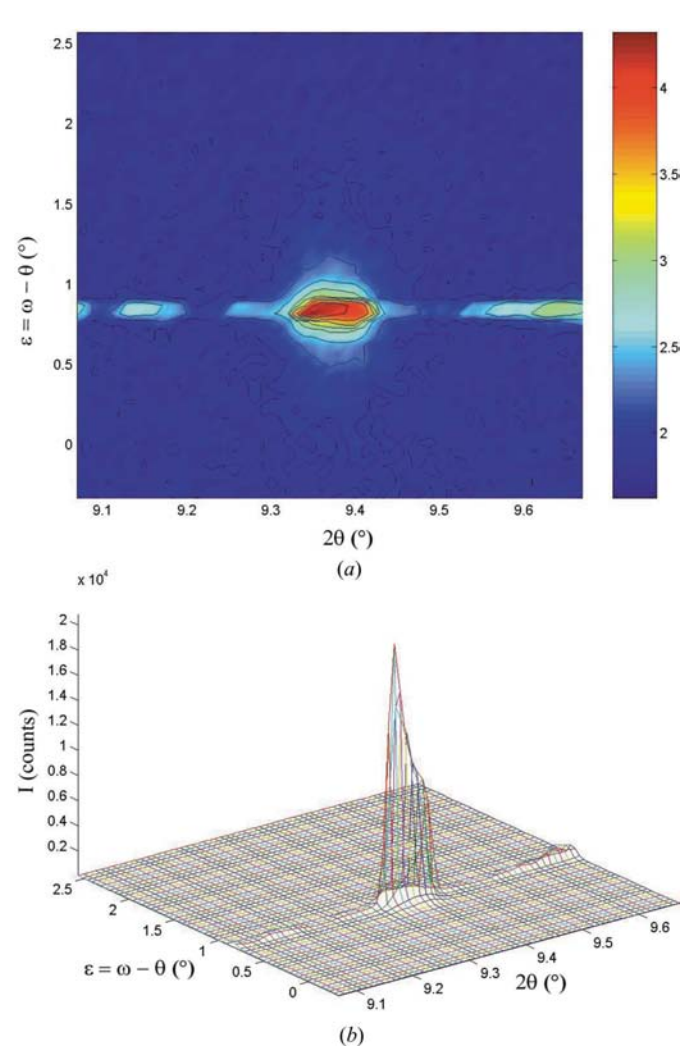
Figure 4
(a) Reciprocal-space map and (b) the corresponding peak profile of the 002 reflection at 8.2 K. The horizontal axis of (a) is the direction of the ω–2θ scan (direction of the diffraction vector) and the vertical axis of (a) is the offset in the ω-scan direction [$\varepsilon = (2\theta/2) - \omega$]. The map was taken at the non-bisecting setting, i.e. $\omega \neq \theta$. The color scale is logarithmic to base 10.

remains almost the same between 100 and 8.2 K. However, if only mosaicity affects the temperature dependence of the intensities, the relative intensities of the peaks should not change dramatically with temperature even if we assume that, because of such angular rearrangement, some peaks superpose and their intensities add. The present data reveal that not only the Bragg angles but also the relative intensities of the peaks at 100 K are dramatically different from the corresponding ones at room temperature. Furthermore, between 100 and 8.2 K the angles remain the same and there is a less dramatic but yet clear change in the relative intensities of the component peaks. These observations imply that the layered mosaic structure of Ce_2RhIn_8 consists of at least two structurally similar phases whose fractions evolve as a function of temperature. Given that the layered structure of Ce_2RhIn_8 is built of structural units of $[CeIn_3]$ and $[RhIn_2]$ and it exhibits planar defects, the two phases can be understood as polytypic phases.

Polytypism (Baumhauer, 1912; Sebastian & Krishna, 1994; Verma & Krisha, 1966) is quite a common phenomenon for layered crystal structures composed of component structural units, as is the structure of Ce_2RhIn_8. Polytypic layered phases are those composed of identical layers (this is only approximately true; for a recent discussion see Trigunayat, 1991) which can be stacked in various ways depending on translation and/or rotation of each layer relative to its neighbors. The various modes of stacking should not affect the composition of each polytypic phase as a whole. As the polytypes of a given compound are composed of virtually identical structural units, their free energies are very similar, so that different polytypes may occur in a stable or metastable state under very similar conditions. As a result, it is virtually impossible to obtain pure samples of a specific polytype. In addition, the very small free-energy differences between different polytypic phases induce phase transformations from one polytypic phase to the other when a control parameter, such as temperature and/or pres-
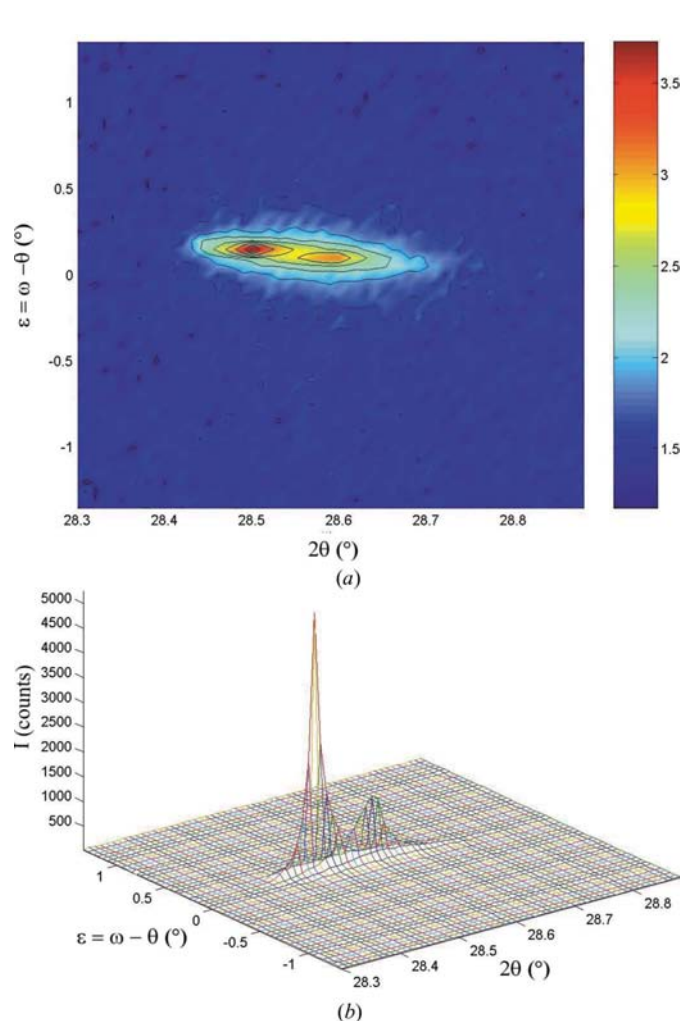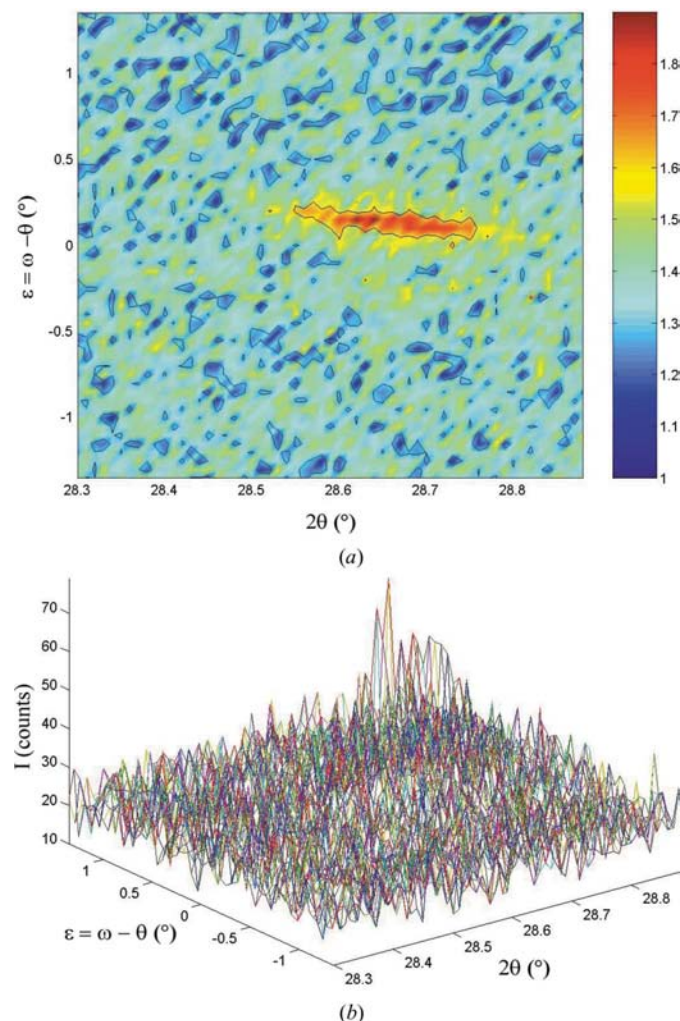

Figure 5
(a) Reciprocal-space map and (b) the corresponding peak profile of the 023 reflection at room temperature. The horizontal axis of (a) is the direction of the ω–2θ scan (direction of the diffraction vector) and the vertical axis of (a) is the offset in the ω-scan direction $[\varepsilon = (2\theta/2) - \omega]$. The map was taken at the non-bisecting setting, i.e. $\omega \neq \theta$. The color scale is logarithmic to base 10.

Figure 6
(a) Reciprocal-space map and (b) the corresponding peak profiles of the 023 reflection at 10 K. The horizontal axis of (a) is the direction of the ω–2θ scan (direction of the diffraction vector) and the vertical axis of (a) is the offset in the ω-scan direction $[\varepsilon = (2\theta/2) - \omega]$. The map was taken at the non-bisecting setting, i.e. $\omega \neq \theta$. The color scale is logarithmic to base 10.

sure, changes. In particular, phase transformations between layered polytypic phases, such as those composing the structure of Ce_2RhIn_8, can be understood as stacking rearrangements (nucleated during the phases transition) and concomitant lattice distortions.

In order to substantiate the conclusions deduced from the reciprocal-space maps of the 002 reflection and gain further insight on the disordered structure of the material we collected reciprocal-space maps of several other hkl reflections. Figs. 5(a), (b) and 6(a), (b) show grid scans surrounding the 023 reflection at room temperature and 10 K, respectively. Obviously, this reflection is less sensitive than the 002 reflection to the planar disorder along the [001] direction and thus no diffuse streaks are present. However, the room-temperature map around the 023 reciprocal lattice point shows two well separated peaks, already observed at the map of the 002 reciprocal lattice point, and which are again signatures of misaligned mosaic blocks. At 10 K, the 023 reflection becomes one very broad and weak peak surrounded by strong diffuse intensity. This observation suggests that the decrease of temperature may reduce the domain misalignment, but causes structural rearrangement and leads to a low-temperature structure with a higher planar-defect density than the room-temperature structure. This remark is consistent with the fact that the diffuse streaks along the [001] direction (Figs. 2–4) become more pronounced at low temperatures.

The dependence on h, k, l of the distribution of the diffuse intensity at the reciprocal-space maps of the various hkl reflections is rationalized in terms of the relative sensitivity of the corresponding hkl planes to the effects of planar defects. For the (00l) reflections stemming from an ordered structure, at each l corresponds a set of equidistant, symmetry-equivalent (parallel among them) 00l planes, which are also parallel to the (ab) plane and intercept the c axis at $1/l, 2/l, \ldots, l - 1/l$. Planar disorder with the planes being perpendicular to the [00l] direction causes line broadening of the 00l reflections and diffuse streaks, as has been illustrated in Figs. 1–4 for the case of the 002 reflection. If we now consider the unit cell of Ce_2RhIn_8 sectioned by the (023) planes then these planes cut several {00l} planes. Consequently, the (023) planes are disrupted by the suggested fault mechanism and so their corresponding maps exhibit peak broadening surrounded by diffuse intensity.

This conclusion and those that have been drawn in the previous paragraphs were based on a comparison of measured intensities (and not of structure factors) at different temperatures. Since the measured intensities are affected from the effects of absorption, Lorentz polarization, extinction and thermal diffuse scattering, it is important to clarify here whether these effects influence the measured intensities to an extent that they affect the reliability of our conclusions. Absorption and Lorentz polarization corrections are temperature independent and consequently the effects of these corrections are equal on the room- and low-temperature intensities. Extinction can vary with temperature if the sample mosaicity changes with temperature, as is indeed the case for Ce_2RhIn_8. However, the extinction correction at both room-

and low-temperature is negligible because of the short wavelength used for our experiments and the disordered state of the material. Thermal diffuse scattering on the other hand is a function of temperature. It influences the Bragg intensities and gives rise to thermal diffuse scattering distributed continuously, but not uniformly throughout reciprocal space. Correction of the thermal diffuse scattering cannot be done for Ce_2RhIn_8 because the calculation requires knowledge of the elastic constants of the material. However, since thermal diffuse scattering is due to the lattice vibrations, its effect is minimized at low temperatures. Consequently, the enhancement of the diffuse scattering around the 023 reflection and of the intensity of the diffuse streaks in the vicinity of the 002 reflection at low temperatures is counter to expectation if we assume that it is due to thermal diffuse scattering. Such an increase in diffuse intensity with decreasing temperature is therefore due to the structural evolution of the disorder in the material, as described in the previous paragraphs.

Finally, it is important to note that the reciprocal-space maps of several other reflections from the 00l family and other hkl families were examined and they reproduce the conclusions drawn above from the 002 and 023 reflections. Also, most of these data were reproduced on a second crystal. In addition, as will be shown in the next paragraphs, the same conclusions were drawn from neutron powder diffraction data taken on several powdered single crystals. Thus, the disorder effects just presented are intrinsic to the material.

4.2. Structure refinement of the high-resolution powder neutron diffraction data

The neutron diffraction data were analysed by the Rietveld method using the General Structure Analysis System (*GSAS*; Larson & Von Dreele, 2001). For the structure refinement we followed two different approaches. First, we started with a simple structural model, *i.e.* a single phase of Ce_2RhIn_8, and refined the structural parameters as well as the profile coefficients. The aim here was to examine first if the powder diffraction data can be modeled by a single-phase model, and second if the profile coefficients reflect the disordered nature of the material and reproduce the effects observed previously by RSM. In the second approach, we chose a starting structural model that fits the real structure effects, *i.e.* a mixture of polytypic phases suggested by the reciprocal-space-mapping study. Then, from the refinement of the structural and profile parameters, we aimed to deduce quantitative information on the real structure of the material. Comparison of the numerical criteria of the fit R_p, R_{wp} and χ^2 and of the diffraction profile fits of the two refinements led us to conclude which model truly describes the structure of the material.

The first structural model used was a single phase of Ce_2RhIn_8 with initial structural parameters taken from Grin *et al.* (1979). Careful inspection of the powder pattern revealed the presence of Al and V peaks from the sample holder; the regions of these peaks were excluded from the pattern. In addition, the powder diagram revealed the presence of the impurity phases Rh, $CeIn_3$ and In. Among these phases, Rh

Table 1
Refined structural parameters at room temperature based on single-phase and two-phase Rietveld refinements described in the text.

Numbers in parentheses are the estimated standard deviations of the last digits. The expression for the anisotropic temperature factor is $\exp[-2\pi^2(a^{*2}U^{11}h^2 + b^{*2}U^{22}k^2 + c^{*2}U^{33}l^2 + 2a^*b^*U^{12}hk + 2a^*c^*U^{13}hl + 2b^*c^*U^{23}kl)]$. U^{ij} ($i, j = 1, 2, 3$) are the tensor components of the mean-square amplitude of anisotropic vibration or displacement parameters.

Parameters	Single-phase model $Ce_{1.86(6)}Rh_{1.01(5)}In_8$ Wt. frac.: 100%	Two-phase model $Ce_{1.80(11)}Rh_{0.98(7)}In_8$ Wt. frac.: 9.55 (42)%	Two-phase model $Ce_{1.88(6)}Rh_{0.97(3)}In_8$ Wt. frac.: 90.45 (42)%
$a = b$ (Å)	4.66516 (4)	4.66325 (18)	4.66548 (5)
c (Å)	12.23763 (21)	12.23875 (51)	12.23778 (26)
V (Å^3)	266.336 (4)	266.148 (18)	266.376 (5)
$x\_Ce = y\_Ce$	0	0	0
z_Ce	0.30662 (34)	0.3059 (13)	0.30674 (36)
$x\_Rh = y\_Rh = z\_Rh$	0	0	0
x_In1	0	0	0
y_In1	0.5	0.5	0.5
z_In1	0.11806 (29)	0.1110 (12)	0.11873 (22)
x_In2	0	0	0
$y\_In2 = z\_In2$	0.5	0.5	0.5
$x\_In3 = y\_In3$	0.5	0.5	0.5
z_In3	0.30369 (48)	0.2940 (18)	0.30472 (48)
U_{iso}_Ce	0.0091 (25)	0.0133 (23)	0.0133 (23)
$U^{11}\_Ce = U^{22}\_Ce$	0.0095 (27)		
U^{33}_Ce	0.0083 (39)		
U_{iso}_Rh	0.0279 (38)	0.0227 (26)	0.0227 (26)
$U^{11}\_Rh = U^{22}\_Rh$	0.0217 (45)		
U^{33}_Rh	0.0403 (79)		
U_{iso}_In1	0.0203 (17)	0.0222 (12)	0.0222 (12)
U^{11}_In1	0.0288 (33)		
U^{22}_In1	0.0115 (34)		
U^{33}_In1	0.0206 (33)		
U_{iso}_In2	0.0217 (17)	0.022 (13)	0.022 (13)
U^{11}_In2	0.0397 (46)		
U^{22}_In2	0.0080 (39)		
U^{33}_In2	0.0173 (35)		
U_{iso}_In3	0.0256 (22)	0.0280 (18)	0.0280 (18)
$U^{11}\_In3 = U^{22}\_In3$	0.0194 (33)		
U^{33}_In3	0.0380 (54)		
Occupancy coefficient_Ce	0.929 (30)	0.899 (57)	0.935 (32)
Occupancy coefficient_Rh	1.009 (46)	0.982 (74)	0.972 (31)
Occupancy coefficient_In1	1 (fixed)	1 (fixed)	1 (fixed)
Occupancy coefficient_In2	1 (fixed)	1 (fixed)	1 (fixed)
Occupancy coefficient_In3	1 (fixed)	1 (fixed)	1 (fixed)
σ_1	146 (19)	430 (44)	167 (11)
γ_1	37 (2)	10 (2)	5.82
γ_2	4 (1)	0	26 (4)
Absorption coefficient	0.309 (19)	0.321 (8)	
R_{wp} (when U_{iso} values are refined)	0.0746	0.0739	
R_{wp} (when U_{aniso} values are refined)	0.074		
R_p (when U_{iso} values are refined)	0.0683	0.0647	
R_p (when U_{aniso} values are refined)	0.0675		
χ^2 (when U_{iso} values are refined)	1.526	1.482	
χ^2 (when U_{aniso} values are refined)	1.504		

shape, which is described in terms of a modified Ikeda–Carpenter function (Ikeda & Carpenter, 1985). This function describes anisotropic broadening effects and is incorporated in the second and third profile functions of *GSAS*. The peak-shape formulation, used in the profile refinement, models several instrumental physical factors, namely pulse shape, moderator physics and instrumental resolution as well as sample effects, namely particle size, strain and planar defects. Thus, the time-of-flight profile function may be described as a multiple convolution of several functions that include Lorentzian and Gaussian contributions. Information about size, strain and stacking fault effects within a sample are contained in the convolution of these two functions and, therefore the peak-shape parameterization is crucial. For the third time-of-flight profile function (Larson & Von Dreele, 2001) used at the present refinement, the Gaussian terms are the profile coefficients σ_0, σ_1 and σ_2, and the Lorentzian terms are the profile coefficients γ_0, γ_1, γ_2, γ_{1e}, γ_{2e}, γ_{2s} and γ_L. The coefficient σ_1 consists of a geometrical contribution from the instrument and the effects of strain in the sample. The coefficient γ_1 is affected mainly by isotropic strain and, to a small extent on HRPD, from instrumental effects. Anisotropic strain influences γ_1 and γ_{1e}. The coefficients γ_2 and γ_{2e} can be used to obtain the particle size. Stacking faults affect the coefficient γ_{2s}.

At the first steps of the refinement only the scale factor and the background coefficients were refined. In the next few cycles, the cell constants of both Ce$_2$RhIn$_8$ and Rh were also refined. After also refining the profile coefficient σ_1 of Ce$_2$RhIn$_8$ and then σ_1 of Rh, we also introduced the impurity phases CeIn$_3$ and In with initial structural parameters taken from Lawrence (1979) and Ridley (1965), respectively. In the next refinement cycles, the following parameters were also refined successively: the fraction of Ce$_2$RhIn$_8$, the fraction of

exhibits the strongest peaks and thus initially, in addition to the single phase of Ce$_2$RhIn$_8$, the Rh phase was also introduced as the second phase. The starting structural parameters of Rh were taken from Singh (1968). The instrumental background was fitted by a Chebyshev polynomial with ten coefficients to be refined. For absorption correction, the second absorption function in *GSAS* was used. This function is useful for the neutron case where the beam suffers substantial absorption, as is the case for our sample. The high-resolution powder diffractometer has a well defined, instrumental line

Table 2
Select interatomic distances and angles at room temperature deduced from the refined atomic positions and cell constants based on the single-phase and the two-phase Rietveld refinements explained in the text.

Numbers in parentheses are the estimated standard deviations of the last digits.

Parameters	Single-phase model $Ce_{1.86 (6)}Rh_{1.01 (5)}In_8$ Wt. frac.: 100%	Two-phase model $Ce_{1.80 (11)}Rh_{0.98 (7)}In_8$ Wt. frac.: 9.55 (42)%	Two-phase model $Ce_{1.88 (6)}Rh_{0.97 (3)}In_8$ Wt. frac.: 90.45 (42)%
$[CeIn_3]$ cuboctahedra			
Interatomic distances (Å)			
Ce—In1 × 4 (out of plane)	3.281 (4)	3.33662 (1)	3.27643 (3)
Ce—IIn2 × 4 (out of plane)	3.3228 (30)	3.32794 (1)	3.32202 (3)
Ce—IIn3 × 4 (in plane)	3.29896 (9)	3.30067 (2)	3.29909 (3)
In2—IIn2 × 4	3.29877 (3)	3.29742 (2)	3.29900 (3)
In3—IIn2 × 4	3.349 (4)	3.43410 (1)	3.33938 (3)
In3—IIn1 × 4	3.256 (5)	3.23336 (1)	3.25939 (3)
Angles (°)			
In1—ICe—IIn1	90.62 (14)	88.662 (0)	90.792 (1)
In1—ICe—IIn1	60.36 (8)	59.224 (0)	60.456 (1)
In2—ICe—IIn2	89.17 (10)	88.954 (0)	89.209 (1)
In2—ICe—IIn2	59.52 (6)	59.394 (0)	59.542 (1)
In3—ICe—IIn3	89.993 (3)	89.997 (0)	89.997 (9)
$[CeIn_3]$ cuboctahedra			
In3—ICe—IIn3	178.75 (29)	174.908 (0)	179.154 (0)
In2—IIn2—IIn2	90.000 (0)	90.000 (0)	90.000 (0)
In2—IIn2—IIn2	179.980 (0)	179.972 (0)	180.000 (0)
$[RhIn_2]$ rectangular parallelepipeds			
Interatomic distances (Å)			
Rh—IIn1 × 8	2.7438 (19)	2.69828 (1)	2.74825 (2)
In1—IIn1 × 4 (parallel to (ab) plane)	3.29877 (3)	3.29742 (2)	3.29900 (3)
In1—IIn1 × 1 (parallel to c axis)	2.890 (7)	2.71607 (1)	2.90599 (5)
Angles (°)			
In1—IRh—IIn1	73.90 (6)	75.327 (0)	73.768 (0)
In1—IRh—IIn1	63.55 (13)	60.437 (0)	63.835 (1)
In1—IIn1—IIn1	90.000 (0)	90.000 (0)	90.000 (0)
In1—IIn1—IIn1	179.980 (0)	179.972 (0)	180.000 (0)

Rh, the profile coefficients γ_1 of Ce_2RhIn_8 and Rh, the profile coefficients σ_1 of $CeIn_3$ and In, the fraction of In and of $CeIn_3$. Among the positional parameters of Ce_2RhIn_8 only the z parameter of Ce, In1 and In3 is not fixed by symmetry and thus this parameter was also varied successively for Ce, In1 and In3. The absorption correction was then applied, through the refinement of the absorption factor of the second absorption function in *GSAS*. Isotropic atomic displacement parameters were also allowed to vary successively for Rh of the Rh phase, for Ce, In1, In3, In2 and Rh of Ce_2RhIn_8, for In of the In phase and for Ce and In of $CeIn_3$. Attempts to model the preferred orientation effects by using the widely employed March–Dollase function (March, 1932; Dollase, 1986) did not considerably improve the fit. On the other hand, when the second preferred orientation correction available in *GSAS*, namely the spherical harmonic function (Von Dreele, 1997), was applied, the residuals were clearly improved. After a few exploratory refinements to determine the sufficient number of harmonic terms that model the preferred orientation effects of our sample, 12 terms were refined together with all other previous parameters. At this stage of the refinement, an anisotropic description of the atomic displacement parameters of the atoms of Ce_2RhIn_8 was introduced. Since all atoms of Ce_2RhIn_8 are on sites of special symmetry, the independent

temperature-factor coefficients for each atom are only U^{11}, U^{22} and U^{33}, which define the major axes of the displacement vibration ellipsoid, while the off-diagonal coefficients U^{12}, U^{13}, U^{23}, defining the orientation of the ellipsoid, are zero (Willis & Pryor, 1975). In the next refinement cycles, the displacement parameters U^{11}, U^{22}, U^{33} were also refined successively for Rh, Ce, In1, In2 and In3. In order to determine the composition of the main phase, Ce_2RhIn_8, the occupancy factors of Ce and then of Rh were refined too. Attempts to refine the occupancy factors of the In1, In2, In3 sites of Ce_2RhIn_8 and of the Ce and In sites of $CeIn_3$ led to values equal to one and consequently these factors were again fixed again to one. Finally, the profile coefficient γ_2 of only the main phase Ce_2RhIn_8 was allowed to vary, but the fit improved only slightly. Attempts to refine other profile coefficients, including γ_{2s}, of the main phase and of the other phases did not lead to any further improvement of the fit. Given that the material exhibits disorder, primary extinction effects should not exist. Indeed, when the extinction coefficient, which is a direct measure of the perfect mosaic block size, was allowed to vary, it took a meaningless value, confirming the disordered nature of the material. The resulted weight fractions of the phases are $Ce_{1.86 (6)}Rh_{1.01 (5)}In_8$: 81.91 (99)%, Rh: 8.90 (73)%, $CeIn_3$: 2.49 (20)%, In: 6.70 (99)%. Table 1 lists the structural parameters of $Ce_{1.86 (6)}Rh_{1.01 (5)}In_8$, the profile coefficients and the absorption coefficient resulted from the refinement, as well as the numerical criteria of the fit (R_p, R_{wp} and χ^2). Selected interatomic distances and angles calculated from the refined cell constants and atomic coordinates are listed in Table 2. The refined structural parameters of the impurity phases are given in the supplementary information of this article.[1]

While the values of the residuals R_p, R_{wp} and χ^2 were quite satisfactory, close examination of the fitted pattern revealed that even though the positions of all the Bragg reflections were well accounted for, particular problems were encountered on

---

[1] Supplementary data for this paper are available from the IUCr electronic archives (Reference: WS5027). Services for accessing these data are described at the back of the journal.

the fit of their peak shape. Figs. 7(a) and 8(a) show two examples of such rather poor fits. Attempts to use other profile functions did not improve the fit. Thus, since the appropriate profile function was used, the observation of poor profile fitting actually questions the adequacy of our model.

In order to explore the possibility of the coexistence of more than one phase, a second series of Rietveld refinement was undertaken. The high resolution and the large accessible range of d spacings of HRPD, in principle, permit the resolution of very similar phases and the determination of their structural parameters, with both high precision, i.e. small standard deviations, and high accuracy, i.e. agreement with the physically correct values (as established by independent measurements). Unconstrained multiphase refinements are therefore viable. The starting model of the new series of refinements consisted of two phases, which have the same weight factions, but differ slightly in their cell constants and atomic coordinates. Correlation effects between the corresponding parameters of the two phases are presumably considerable because of the extensive overlap of the two phases. It is therefore important that the starting values of the structural parameters are as accurate as possible. As the starting values for the first phase we used the values of the structural parameters of Ce_2RhIn_8 obtained from the refinement of the single-phase model. For the second phase several starting structural parameters were tested through exploratory refinements. It was found that the starting parameters of the second phase, that allow stable refinements resulting in physically meaningful values, must be very close but not equal to the corresponding ones of the first phase. The following starting values for the parameters of the second phase were used: $a = 4.666$, $c = 12.23$ Å, $z\_Ce = 0.3$, $z\_In1 = 0.11$, $z\_In3 = 0.3$ and occupancy coefficients equal to 1, for all atoms. The initial values of the displacement factors of the atoms of the second phase were taken to be equal to the corresponding ones of the first phase. The impurity phases Rh, $CeIn_3$ and In were also introduced in the two-phase model similarly as done previously for the single-phase model. In the first steps, only the scale factor and the ten background coefficients were refined. In the next cycles the cell constants of both phases were refined. The profile coefficient σ_1 of the first phase was initially constrained to be equal with σ_1 of the second phase, and refined in the next cycles. The constraint was then removed and σ_1 of the first phase, and subsequently σ_1 of the second one were refined independently. The fraction of the first and then of the second phase were also refined next. In the following cycles, the z parameter of Ce, In1 and In3 of the first and then of the second phase were refined one by one. After refining the absorption coefficient, the isotropic displacement factors of Ce, Rh, In1, In2, In3 of both phases were refined successively. Subsequent attempts to improve the fit by refining the profile coefficient γ_1, as well as the other profile coefficients of both phases, proved unsuccessful. However, only the coefficient γ_1 (which is affected by strain) of the first phase and the coefficient γ_2 (which is a measure of the mosaic block size) of the second phase were found to take meaningful values. Preferred orientation effects for the first, then for the

second phase, were also corrected by applying the same preferred orientation function as at the refinement of the single-phase model. At this stage of the refinement, various models of disorder for either the first phase or the second one, or for both phases were tested, for example, substitution of Ce at the Rh sites and vice versa, partially occupied In planes. They all led to significantly poorer fits and increased values of the residuals. It must be noted here that the neutron scattering lengths of Ce, Rh and In are 4.84, 5.88 and 4.065 fm, respectively, and thus the lack of significant contrast between them makes the determination of any degree of site disorder difficult. The fact, however, that no modulated diffuse scattering among the Bragg peaks, other than the diffuse streaks due to planar defects, was observed either at the synchrotron X-ray reciprocal-space maps or at the electron diffraction patterns confirms that no anti-site disorder occurs. In the next cycles, the constraints that imposed the displacement factors of the atoms of the first phase to be equal to the corresponding ones of the second phase were removed and the displacement factors of the atoms of each phase were refined independently. Their corresponding values remained almost equal within their standard deviations. Owing to the complexity of the model and the increase in the number of the parameters to be refined, it was not possible to refine the anisotropic displacement factors of all atoms of all five phases. In the last refinement cycles, the occupancy coefficients of Ce and of Rh of the first and then of the second phase were refined one by one. The final results of the refinement are listed in Table 1. The weight fractions of the phases are: $Ce_{1.80\,(11)}Rh_{0.98\,(7)}In_8$: 7.87 (42)%, $Ce_{1.88\,(6)}Rh_{0.97\,(3)}In_8$: 74.57 (41)%, Rh: 8.7 (7)%, $CeIn_3$: 2.4 (3)% and In: 6.5 (9)%. The diffraction profile is shown in Fig. 9. Expanded regions of the diffraction profile are shown in Figs. 7(b) and 8(b). Selected interatomic distances and angles calculated from the refined cell constants and atomic coordinates are given in Table 2.

It is clear that, compared with the single-phase model, the two-phase model results in an improved diffraction-profile fit and slightly lower values of R_p, R_{wp} and χ^2. The structure of Ce_2RhIn_8 is therefore better described as a complex mixture of two tetragonal polytypic phases, $Ce_{1.88\,(6)}Rh_{0.97\,(3)}In_8$ and $Ce_{1.80\,(11)}Rh_{0.98\,(7)}In_8$, with weight fractions 90.45 (42)% and 9.55 (42)%, respectively. Both phases are slightly Ce-deficient and one or both phases are possibly also Rh-deficient, but no definitive conclusion can be drawn on the exact deficiencies, because the Ce and Rh contents of both phases are (within three times their standard deviations) almost equal to the stoichiometric values. Both phases have the same tetragonal structure, but most of their structural parameters are different. The a cell parameter of the minority phase is clearly smaller than the corresponding one of the majority phase, but their corresponding c parameters are almost equal (within three times their standard deviations). Consequently, the cell volume of the minority phase is smaller than that of the majority phase. Lower Ce content in the minority phase could cause volume contraction, however, it is not clear from the occupancy factors of Ce that the Ce content is indeed lower in the minority phase. The difference

in volume most probably is due to more defects in the minority phase, which create higher strain (obviously compressive) and concomitant lattice distortions and volume contraction. Indeed, the profile coefficients σ_1 and γ_1, which are sensitive to strain effects, are clearly higher for the minority phase, implying that the average value of the strain in the minority phase is about twice that in the majority phase. In contrast, since the profile coefficient γ_2 of the minority phase is much smaller than γ_2 of the majority phase, the average domain size of the minority phase is higher that the average size of the mosaic blocks of the majority phase. Obviously, the lattice response to local strain is not only elastic, but also plastic deformation, *i.e.* depending on the value of the local strain, the lattice simply fragments to produce smaller less strained segments. Thus, the majority phase displays rather small, less

strained mosaic blocks compared with the minority phase that is built by large, more strained mosaic blocks. This conclusion is consistent with the observation by reciprocal-space mapping that the material adopts a mosaic structure composed mainly of small and well aligned blocks disrupted by larger and more tilted blocks with different lattice parameters from the small ones.

Turning now to the structural distortions, it is remarkable that some crystallographic planes are almost at the same z position for both phases, but the positions of other planes are clearly different in the two phases. For both phases the Ce planes are almost at the same z position [$z\_Ce = 0.30674\,(36)$ for the majority phase and $z\_Ce = 0.3059\,(13)$ for the minority one]. Similarly, the In2 planes, which are the common planes of two consecutive [CeIn$_3$] layers, are for both phases at the
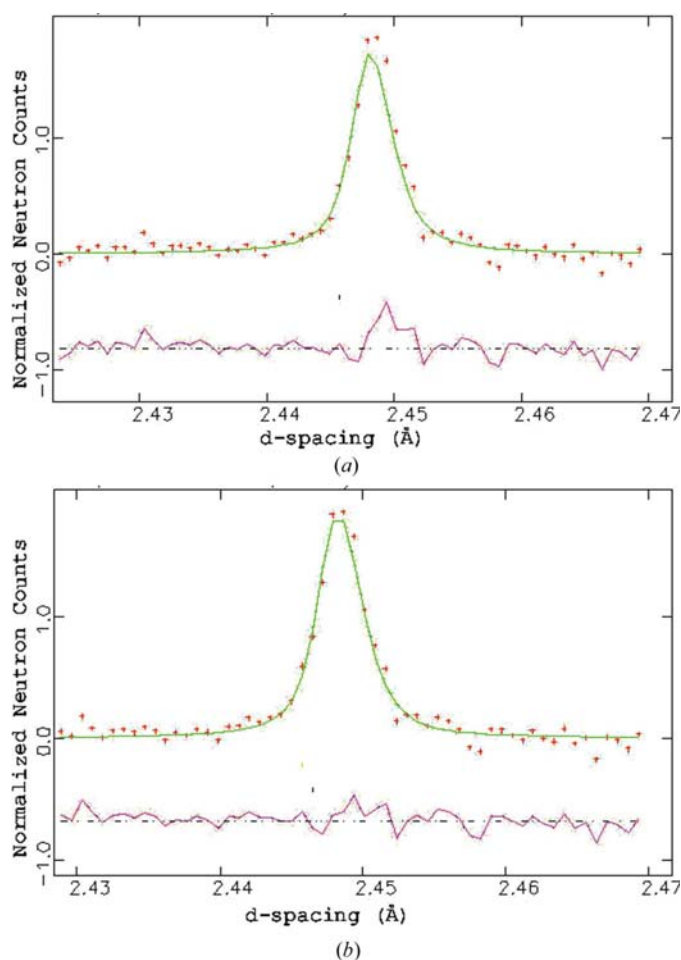

Figure 7
Expanded region of the diffraction profile from 2.43 to 2.47 Å corresponding to the 005 reflection for the two structural models explored in this study: (*a*) single phase and (*b*) two-phase model. Crosses are experimental points; green solid lines are calculated patterns from full-profile Rietveld refinements, and pink solid lines are difference curves (observed minus calculated). In (*a*), the black vertical tick mark represents the calculated peak position of the 005 reflection of the single phase. In (*b*) the yellow and black vertical tick marks represent the calculated peak positions of the 005 reflection of the majority and minority phase, respectively.
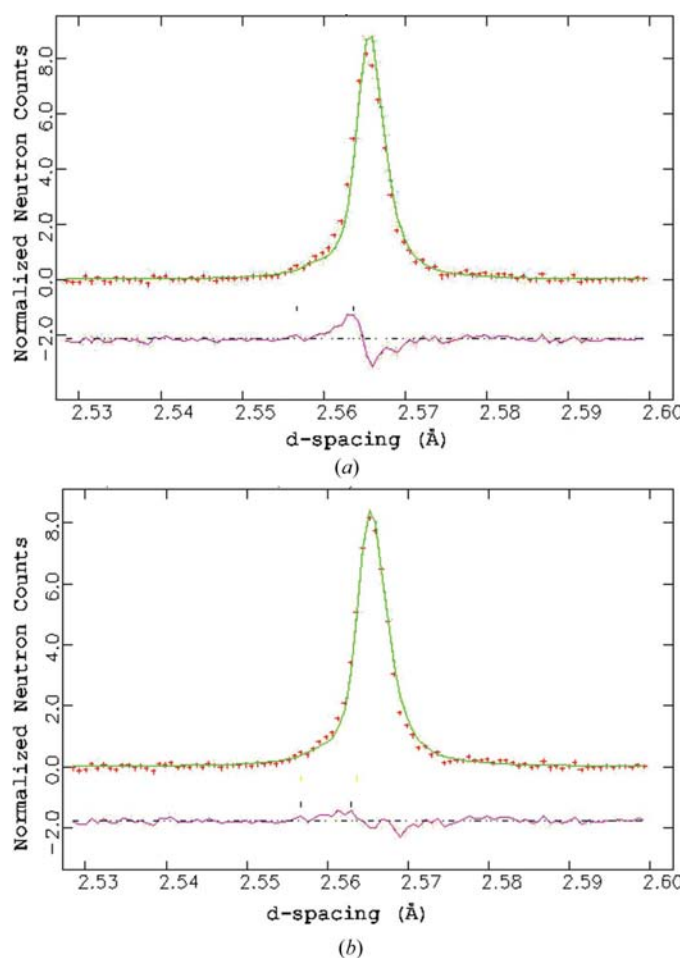
Figure 8
Expanded region of the diffraction profile from 2.53 to 2.60 Å containing the 014 and 113 reflections for the two structural models explored in this study: (*a*) single-phase and (*b*) two-phase model. The 014 reflection is the very weak one at $d = 2.558$ Å and 113 is the strong reflection at $d = 2.565$ Å. Crosses are experimental points; green solid lines are calculated patterns from full-profile Rietveld refinements, and pink solid lines are difference/e.s.d. curves (observed minus calculated). In (*a*) the black vertical tick mark represents the calculated peak positions of the 014 and 113 reflections of the single phase. In (*b*) the yellow vertical tick marks represent the calculated peak positions of the 014 and 113 reflections of the majority phase and the black vertical tick marks represent the calculated peak positions of the 014 and 113 reflections of the minority phase.

same position, $z\_In2 = 0.5$, fixed by the symmetry. However, the In1 planes, which are the common planes of the [CeIn$_3$] and the [RhIn$_3$] layers, are at different positions in the two phases [$z\_In1 = 0.11873$ (22) for the majority phase compared with $z\_In1 = 0.1110$ (12) for the minority one]. Even more dramatic is the displacement of the In3 layers in the minority phase from their position in the majority phase [$z\_In3 = 0.30472$ (48) for the majority phase and $z\_In3 = 0.2940$ (18) for the minority phase]. As a result of these displacements, the [CeIn$_3$] cuboctahedra and the [RhIn$_2$] rectangular parallelepipeds of the majority phase are compressed and expanded, respectively, compared with the corresponding polyhedra of the minority phase. However, the compression of the [CeIn$_3$] cuboctahedra in the majority phase is not uniform, resulting in severely distorted cuboctahedra, elongated towards their adjacent [CeIn$_3$] layer. In addition, from the angles In2—In2—In2 = 180.000 (0)° and In1—In1—In1 = 180.000 (0)°, it is deduced that the [CeIn$_3$] cuboctahedra and the [RhIn$_2$] parallelepipeds, each within their own layer, are well aligned in the majority phase. However, this is not the case for the corresponding polyhedra of the minority phase, which are clearly misaligned, as demonstrated from the angles In2—In2—In2 = 179.972 (0)° and In3—In3—In3 = 179.972 (0)°. Furthermore, within each [CeIn$_3$] cuboctahedron there is an important difference in the angle In3—Ce—In3, which is 174.908 (0)° in the minority phase, compared with 179.154 (0)° in the majority phase and to 180° for the ideal CeIn$_3$ cuboctahedron. This is due to the fact that the Ce layer is about six times higher from the In3 layer in the minority phase than it is

in the majority phase, while in the ideal non-distorted CeIn$_3$ cuboctahedron the Ce and In3 layers coincide. Also, in CeRhIn$_5$ these two layers coincide, since its [CeIn$_3$] cuboctahedra are simply compressed from their adjacent [RhIn$_2$] layers.

Finally, we note that attempts to refine the data by using a three-phase model did not lead to any further improvement of the fit. The number of parameters to be refined was no more manageable and it was not possible to refine all of them independently.

5. Concluding remarks

The crystal structure of Ce$_2$RhIn$_8$ is a complex mixture of two layered, mosaic, polytypic phases affected by non-periodic partially correlated planar defects. Both phases adopt the same tetragonal structure, but they differ in their structural parameters and (eventually) compositions, size and tilt angles of their mosaic blocks, and strain. Such lattice disorder results in broken translation symmetry and thus affects the low-temperature properties of the material.

The high-resolution neutron powder diffraction data are well represented by a two-phase structural model, *i.e.* a bimodal distribution of crystallographic parameters. However, it must be noted here that the two values of each crystallographic parameter can simply be the lower and higher ones, and intermediate values (of other phases with very low but non-zero intensity) cannot be excluded. The bimodal distribution of lattice parameters, and the presence of random planar defects and position-dependent mosaicity and strain imply that Ce$_2$RhIn$_8$ approaches the paracrystalline state (Hosemann, 1949, 1950a,b; Hindeleh & Hosemann, 1988) rather than the crystalline state. Within the paracrystal formalism, translation and symmetry operators are coupled with probability operators and thus, paracrystals allow fluctuations of lengths and orientations of lattice vectors. The paracrystalline state has been observed at ambient or non-ambient conditions in a wide variety of adaptive materials, including biological systems, polymers, transition metal oxides (with perovskite or spinel structure), metals and alloys. However, to our knowledge, it is the first time that the lattice of a heavy fermion material is found to approach a paracrystalline
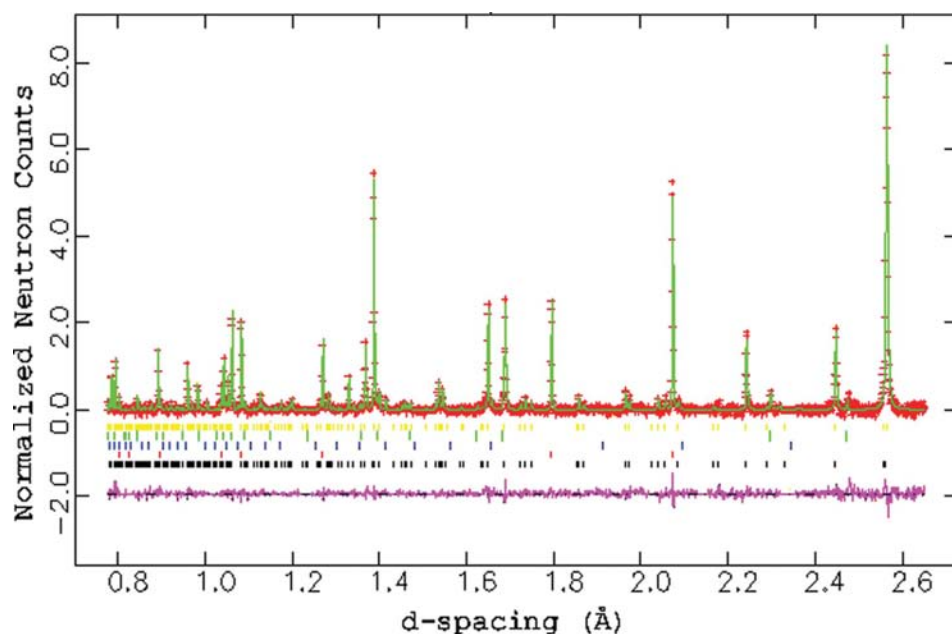

Figure 9
Observed (crosses), calculated (green line) and difference (pink line) neutron powder diffraction profile. The yellow and black vertical tick marks represent the calculated peak positions of the majority Ce$_{1.88\,(6)}$Rh$_{0.97\,(3)}$In$_8$ phase and for the minority Ce$_{1.80\,(11)}$Rh$_{0.98\,(7)}$In$_8$ phase, respectively. The red, blue and green vertical tick marks represent the calculated peak positions of the impurity phases Rh, CeIn$_3$ and In, respectively. Some impurity peaks are quite strong, for example, the 111 reflection of the Rh impurity at $d = 2.081$ Å.

state rather than a classic crystalline state. Whether this material is a true paracrystal, *i.e.* if it can be modeled by using the statistical basis of paracrystallinity, remains to be explored. In addition, Ce_2RhIn_8 is the first heavy fermion compound found to exhibit an intricate coexistence and segregation of two chemically and structurally distinct disordered phases at ambient conditions. Coexisting superconducting and/or magnetic phases have been found in a few (presumably structurally homogeneous) heavy fermion systems, but only at their ground state. Such phases were induced by a control parameter such as temperature, pressure or magnetic field and, in the case of coexisting superconducting phases, were attributed to different pairing mechanisms or symmetries.

While further low-temperature/medium-pressure diffraction experiments would be valuable to establish an accurate structure–property relationship in Ce_2RhIn_8, the crystallographic results of the present study unravelled a fascinating structural chemistry and an intricate lattice disorder behind the physics of this remarkable material. Whether this structural chemistry can be tuned by synthetic conditions remains an open interesting question.

References

Aeppli, G. & Fisk, Z. (1992). *Commun. Condens. Matter Phys.* **16**, 155–165.

Arndt, U. W. & Willis, B. T. M. (1966). *Single Crystal Diffractometry*, pp. 37–52. Cambridge University Press.

Bao, W. (2005). Personal communication.

Bao, W., Pagliuso, P. G., Sarrao, J. L., Thompson, J. D., Fisk, Z. & Lynn, J. W. (2001). *Phys. Rev. B*, **64**, 0204011-4(R).

Baruchel, J., Hodeau, J. L., Lehmann, M. S., Regnard, J. R. & Schlenker, C. (1993). Editors. *Neutron and Synchrotron Radiation for Condensed Matter Studies, Higher European Research Course for Users of Large Experimental Systems*, Vol. I, Les Editions de Physique, pp. 179–191. Berlin: Springer-Verlag.

Baumhauer, H. (1912). *Z. Kristallogr.* **50**, 33–39.

Bernal, O. O., MacLaughlin, D. E., Lukefahr, H. G. & Andraka, B. (1995). *Phys. Rev. Lett.* **75**, 2023–2026.

Brock, C. P., Craven, B. M., Frenz, E., Gabe, B. A., Sparks, R. A., Strouse, C. E., Trueblood, K. N. & Wang, B. C. (1995). *Lecture Notes for the Summer School 'Course for Crystallographers': Structure Analysis by X-ray Crystallography*, pp VII 1–7. 2–15 August 1995, Pittsburgh, Pennsylvania, USA.

Brockhouse, B. N. (1955). *Phys. Rev.* **99**, 601–603.

Canfield, P. C. & Fisk, Z. (1992). *Philos. Mag. B*, **65**, 1117–1123.

Castro Neto, A. H., Castilla, G. & Jones, B. A. (1998). *Phys. Rev. Lett.* **81**, 3531–3534.

Castro Neto, A. H. & Jones, B. A. (2000). *Phys. Rev. B*, **62**, 14975–15011.

Collins, S. P., Cernik, R. J., Fell, B., Tang, C. C., Harris, N. W., Miller, M. C. & Oszlanyi, G. (1998). *J. Synchrotr. Rad.* **5**, 1263–1269.

Collins, S. P., Murphy, B. M., Tang, C. C., Miller, M. C. & Oszlanyi, G. (1999). *J. Phys. D Appl. Phys.* **32**, A81–A83.

Cornelius, A. L., Pagliuso, P. G., Hundley, M. F. & Sarrao, J. L. (2001). *Phys. Rev. B*, **64**, 1444111-4.

Dollase, W. A. (1986). *J. Appl. Cryst.* **19**, 267–272.

Fewster, P. F. (1997). *Crit. Rev. Solid State Mater. Sci.* **22**, 69–110.

Fisk, Z., Hess, D. W., Pethick, C. J., Pines, D., Smith, J. L., Thompson, J. D. & Willis, J. O. (1988). *Science*, **239**, 33–42.

Fisk, Z., Ott, H. R. & Smith, J. L. (1987). *J. Less Common Met.* **133**, 99–106.

Fisk, Z., Sarrao, J. L., Smith, J. L. & Thompson, J. D. (1995). *Proc. Natl. Acad. Sci.* **92**, 6663–6667.

Fisk, Z. & Remeika, J. P. (1989). *Handbook on the Physics and Chemistry of Rare Earths*, edited by K. A. Gschneider & L. Eyring, Vol. 12, pp. 53–70. Amsterdam: Elsevier Science Ltd.

Fisk, Z., Thompson, J. D. & Ott, H. R. (1988). *J. Magn. Magn. Mater.* **76/77**, 637–641.

Grewe, N. & Steglich, F. (1991). *Handbook on the Physics and Chemistry of the Rare Earths*, edited by K. A. Gschneidner & L. Eyring, Vol. 14, pp. 343–474. Amsterdam: Elsevier Science Ltd.

Grin, Y. N., Yarmolyuk, Y. P. & Giadyshevskii, E. I. (1979). *Sov. Phys. Crystallogr.* **24**, 137–139.

Hegger, H., Petrovic, C., Moshopoulou, E. G., Hundley, M. F., Sarrao, J. L., Fisk, Z. & Thompson, J. D. (2000). *Phys. Rev. Lett.* **84**, 4986–4989.

Hindeleh, A. M. & Hosemann, R. Z. (1988). *J. Phys. C Solid State Phys.* **21**, 4155–4170.

Hosemann, R. Z. (1949). *Z. Phys.* **127**, 16–39.

Hosemann, R. Z. (1950a). *Z. Phys.* **128**, 1–35.

Hosemann, R. Z. (1950b). *Z. Phys.* **128**, 465–492.

Ibberson, R. M., David, W. I. F. & Knight, K. S. (1992). The High Resolution Neutron Powder Diffractometer (HRPD) at ISIS – A User Guide Report RAL-92-031.

Ikeda, S. & Carpenter, J. M. (1985). *Nucl. Instrum. Methods A*, **239**, 536–544.

King, R. B. (1997). *J. Solid State Chem.* **131**, 394–398.

Larson, A. C. & Von Dreele, R. B. (2001). *General Structure Analysis System*, LAUR 86-748. Los Alamos National Laboratory, New Mexico, USA.

Lawrence, J. (1979). *Phys. Rev. B*, **20**, 3770–3782.

Lengyel, E., Sarrao, J. L., Sparn, G., Steglich, F. & Thompson, J. D. (2004). *J. Magn. Magn. Mater.* **272–276**, 52–53.

Llobet, A., Gardner, J. S., Moshopoulou, E. G., Mignot, J.-M., Nicklas, M., Bao, W., Moreno, N. O., Pagliuso, P. G., Goncharenko, I. N., Sarrao, J. L. & Thompson, J. D. (2004). *Phys. Rev. B*, **69**, 0244031-6.

Macaluso, R. T., Sarrao, J. L., Moreno, N. O., Pagliuso, P. G., Thompson, J. D., Fronczek, F. R., Hundley, M. F., Malinowski, A. & Chan, J. Y. (2003). *Chem. Mater.* **15**, 1394–1398.

Malinowski, A., Hundley, M. F., Moreno, N. O., Pagliuso, P. G., Sarrao, J. L. & Thompson, J. D. (2003). *Phys. Rev. B*, **68**, 1844191-12.

March, A. (1932). *Z. Kristallogr.* **81**, 285–297.

Marthur, N. D., Groch, F. M., Julian, S. R., Walker, I. R., Freye, D. M., Hasselwimmer, R. K. W. & Lonzarich, G. G. (1998). *Nature*, **394**, 39–43.

Miranda, E. & Dobrosavljevic, V. (2001). *Phys. Rev. Lett.* **86**, 264–267.

Miranda, E., Dobrosavljevic, V. & Kotliar, B. G. (1996) *J. Phys. Condens. Matter*, **8**, 9871–9900.

Miranda, E., Dobrosavljevic, V. & Kotliar, B. G. (1997). *Phys. Rev. Lett.* **78**, 290–293.

Morris, G. D., Heffner, R. H., Moreno, N. O., Pagliuso, P. G., Sarrao, J. L., Dunsiger, S. R., Nieuwenhuys, G. J., MacLaughlin, D. E. & Bernal, O. O. (2004). *Phys. Rev. B*, **69**, 2144151-6.

Moshopoulou, E. G., Fisk, Z., Sarrao, J. L. & Thompson, J. D. (2001). *J. Solid State Chem.* **158**, 25–33.

Moshopoulou, E. G., Prokes, K., Garcia-Matres, E., Pagliuso, P. G., Sarrao, J. L. & Thompson, J. D. (2002). *Physica B*, **318**, 300–305.

Moshopoulou, E. G., Sarrao, J. L., Pagliuso, P. G., Moreno, N. O., Thompson, J. D., Fisk, Z. & Ibberson, R. M. (2002). *Appl. Phys. A Mater. Sci. Proc.* **74**, S895–S897.

Murphy, B. M., Collins, S. P., Golshan, M., Moore, M., Reid, J. & Kowalski, G. (2001). *Nucl. Instrum. Methods Phys. Res. A*, **467**, 1014–1018.

Nave, C. (1998). *Acta Cryst.* D**54**, 848–853.

Nicklas, M., Sidorov, V. A., Borges, H. A., Pagliuso, P. G., Petrovic, C., Fisk, Z., Sarrao, J. L. & Thompson, J. D. (2003). *Phys. Rev. B*, **67**, 0205061-4(R).

Ohara, S., Shomi, Y. & Sakamoto, I. (2003). *Physica B*, **329–333**, 612–613.

Ott, H. R. & Fisk, Z. (1989). *ACS Symp. Ser.* **394**, 260–272.

Pick, M. A., Bickmann, K., Pofahl, E., Zwoll, K. & Wenzl, H. (1977). *J. Appl. Cryst.* **10**, 450–457.

Ridley, N. (1965). *J. Less-Common Met.* **8**, 354–357.

Schwartz, L. H. & Cohen, J. B. (1987). *Diffraction from Materials*, 2nd ed. Berlin: Springer Verlag.

Sebastian, M. T. & Krishna, P. (1994). *Random, Non-Random and Periodic Faulting in Crystals.* Yverdon, Switzerland, Langhorne, Pennsylvania, USA: Gordon and Breach.

Singh, H. P. (1968). *Acta Cryst.* A**24**, 469–471.

Stewart, G. R. (1984). *Rev. Mod. Phys.* **56**, 755–787.

Stout, G. H. & Jensen, L. H. (1989). *X-ray Structure Determination*, 2nd ed., pp. 132–136. New York: John Wiley and Sons.

Takahashi, I., Kagayama, A., Oomi, G., Onuki, Y. & Komatsubara, T. (1999). *Acta Cryst.* B**55**, 31–34.

Thompson, J. D. & Lawrence, J. M. (1994). *Handbook on the Physics and Chemistry of the Rare Earths*, Vol. 19, edited by K. A. Gschneidner, L. Eyring, G. H. Lander & G. R. Chopin, pp. 383–477. Amsterdam: Elsevier.

Thompson, J. D., Movshovich, R., Fisk, Z., Bouquet, F., Curro, N. J., Fisher, R. A., Hammel, P. C., Hegger, H., Hundley, M. F., Jaime, M., Pagliuso, P. G., Petrovic, C., Philips, N. E. & Sarrao, J. L. (2001). *J. Magn. Magn. Mater.* **226–230**, 5–10.

Trigunayat, G. C. (1991). *Solid State Ion.* **48**, 3–70.

Ueda, T., Shishido, H., Hashimoto, S., Okubo, T., Yamada, M., Inada, Y., Settai, R., Harima, H., Galatanu, A., Yamamoto, E., Nakamura, N., Sugiyama, K., Takeuchi, T., Kindo, K., Namiki, T., Aoki, Y., Sato, H. & Onuki, Y. (2004). *J. Phys. Soc. Jpn*, **73**, 649–655.

Verma, A. R. & Krisha, P. (1966). *Polymorphism and Polytypism in Crystals.* New York: John Wiley and Sons.

Von Dreele, R. B. (1997). *J. Appl. Cryst.* **30**, 517–525.

Willis, B. T. M. & Pryor, A. W. (1975). *Thermal Vibrations in Crystallography*, pp. 102–110. Cambridge University Press.